1 **Two-photon calcium imaging of medial prefrontal cortex and hippocampus**

2 **without cortical invasion**

3

4 Masashi Kondo[1,2], Kenta Kobayashi[3], Masamichi Ohkura[4], Junichi Nakai[4], and Masanori

5 Matsuzaki[1,2]

6

7 [1]Department of Physiology, Graduate School of Medicine, The University of Tokyo, Tokyo,

8 Japan

9 [2]Division of Brain Circuits, National Institute for Basic Biology, Okazaki, Japan

10 [3]Section of Viral Vector Development, National Institute for Physiological Sciences, Okazaki,

11 Japan

12 [4]Brain Science Institute, Saitama University, Saitama, Japan

13

14

15 Corresponding author: Professor Masanori Matsuzaki, Ph.D.

16 Address: Department of Physiology, Graduate School of Medicine, The University of Tokyo,

17 7-3-1, Hongo, Bunkyo-ku, Tokyo, 113-0033, Japan

18 Tel: +81-3-5841-3471

19 Fax: +81-3-5841-3471

20 E-mail: mzakim@m.u-tokyo.ac.jp

21

22

23

24   **Abstract**

25   *In vivo* two-photon calcium imaging currently allows us to observe the activity of

26   multiple neurons up to ~900 μm below the cortical surface without cortical invasion.

27   However, many other important brain areas are located deeper than this. Here, we used

28   a 1100 nm laser, which underfilled the back aperture of the objective, and red

29   genetically encoded calcium indicators to establish two-photon calcium imaging of the

30   intact mouse brain and detect neural activity up to 1200 μm from the cortical surface.

31   This imaging was obtained from the medial prefrontal cortex (the prelimbic area) and

32   the hippocampal CA1 region. We found that the neural activity related to reward

33   prediction is higher in the prelimbic area than in layer 2/3 of the secondary motor area,

34   while it is negligible in the hippocampal CA1 region. Reducing the invasiveness of

35   imaging is an important strategy to reveal the brain processes active in cognition and

36   memory.

37

Introduction

39   Two-photon calcium imaging reveals the *in vivo* activity of multiple neurons at a cellular and

40   subcellular resolution (Jia et al., 2010; Ohki et al., 2005). Recent work demonstrated that, by

41   exciting red-fluorescent calcium indicators with a laser at wavelengths of 1000–1100 nm, it is

42   possible to image neural activity in the mouse sensory cortex at depths of 800–900 μm from

43   the cortical surface attached to a cranial window (corresponding to layers 5 and 6) (Dana et

44   al., 2016; Tischbirek et al., 2015). However, for functional imaging of deeper regions, such as

45   the medial prefrontal cortex, hippocampus, and basal ganglia, it has been reported that

46   invasive penetration is unavoidable; it is necessary to insert a microlens or a microprism into

47   the cortical tissue, or remove the cortical tissue above the target region (Attardo et al., 2015;

48   Dombeck et al., 2010; Low et al., 2014; Pilz et al., 2016). In this study, we demonstrate that,

49   by shortening the light-path length within the tissue to reduce light scattering (Helmchen and

50   Denk, 2005) and exciting red-fluorescent genetically encoded calcium indicators (red GECIs;

51   Dana et al., 2016; Ohkura et al., 2015), we could detect the activity of multiple neurons in the

52   medial prefrontal cortex (the prelimbic [PL] area) and hippocampal CA1 region at depths of

53   1.0–1.2 mm in behaving mice, without the need for invasive penetration or removal of

54   cortical tissue.

55

56   **Results and Discussion**

57   The light-path length within the tissue was shortened by reducing large-angle rays emitting

58   from an objective with high numerical aperture (1.05 or 1.00). To do so, the back aperture of

59   the objective was underfilled with a diameter-narrowed laser beam (7.2 mm, in comparison

60   with that of the back aperture of 15.1 mm or 14.4 mm) (Helmchen and Denk, 2005;

61   Matsuzaki et al., 2008) at a wavelength of 1100 nm. Three to four weeks after an injection of

62   adeno-associated virus (AAV) carrying the R-CaMP1.07 gene into the intact medial frontal

63   cortex (mFrC) of 2–3-month-old mice, we observed R-CaMP1.07-expressing neurons in the

64   mFrC at depths of 100–1200 μm from the cortical surface, in awake and head-restrained mice

65   (Figure 1a, b and Video 1). Using a laser intensity of 170–180 mW under the objective, we

66   could detect calcium transients at depths of 1.0–1.2 mm (Figure 1c). Cell death, severe

67   inflammation, and heating-induced responses were not apparent on histological staining after

68   long-term imaging of the mFrC (Figure 1d–g). This is consistent with a study that reported

69   that heat-induced cell responses occur when the laser intensity exceeds 300 mW (Podgorski

70   and Ranganathan, 2016).

71   We next examined whether neural activity in the hippocampus can be imaged

4

72   without removal of the neocortical tissue lying above it (Figure 2a). CA1 GFP-expressing

73   neurons can be detected by two-photon microscopy in 4-week-old mice, but not in 6- to

74   9-week-old mice (Kawakami et al., 2013). We therefore injected AAV-jRGECO1a into the

75   hippocampus of mice aged between 12 and 14 days, and then performed imaging after

76   another 2 weeks. When we deepened the focal plane below the white matter to depths of

77   900–1000 μm, we observed densely distributed fluorescent neurons typically located in CA1

78   pyramidal layer (Figure 2b, c and Video 2), as described previously (Dombeck et al., 2010),

79   and clearly detected spontaneous calcium transients from these neurons (Figure 2c). No cell

80   death or strong damage was apparent after 15 min of imaging (Figure 2d, e). By contrast, we

81   could not detect any neural activity in the CA1 region of the mice when they were 3 months

82   old. To image neural activity in the hippocampus or the infralimbic area of adult mice, it is

83   necessary to use higher average power of the laser or higher peak power per pulse than that

84   used in this study (Kawakami et al., 2015). In addition, adaptive optics (Ji et al., 2010) and

85   further improvement of red GECIs (Dana et al., 2016; Inoue et al., 2014) will certainly be

86   helpful.

87   To demonstrate the utility of this method for identifying neural functions in deep

88   areas in the intact brain, we examined reward prediction-related activity in the mFrC over ~1

5

89   mm depth, as the mFrC demonstrates strong activity before movement starts (Friedman et al.,

90   2015; Kim et al., 2016; Pinto and Dan, 2015; Sul et al., 2011). Head-restrained mice were

91   conditioned to the delivery of a drop of water with an inter-delivery interval of 20 s (Figure

92   3a). As each session progressed (one session per day), the lick response to the water delivery

93   increased in rate and became faster (Figure 3a–d). From the fifth session onwards, we

94   performed two-photon calcium imaging of the mFrC at cortical depths of 100–1200 μm

95   (Video 3). The imaging fields were classified into three areas according to depth (Paxinos and

96   Franklin, 2007): the superficial area (100–300 μm, corresponding to layer 2/3 in the

97   secondary motor area, M2), middle area (300–800 μm, corresponding to layer 5 in M2), and

98   deep area (800–1200 μm, roughly corresponding to layer 6 in M2 and the PL area). In all

99   three areas, approximately 50% of neurons showed a peak of mean (trial-averaged) activity

100   during 5 s after the water delivery (Figure 3e, f), which was presumably related to licking and

101   water acquisition (Figure 3b). Additionally, approximately 30% of neurons in all three areas

102   showed a peak mean activity during 10 s before the water delivery (pre-reward period). The

103   sequential distribution of the times of peak activity was not an artifact of ordering the neurons

104   according to the time of peak activity, as the ratio of the mean activity around the peak

105   activity to the baseline activity (ridge-to-background ratio; Harvey et al., 2012) was

6

106   significantly higher than that of shuffled data (Figure 3g, h). Additionally, the sequential

107   distribution of neurons with peak activity during the pre-reward period was not an artifact

108   (Figure 3–Figure supplement 1). Even when 5 s windows were chosen from the pre-reward

109   period, the ridge-to-background ratios of deep-area neurons with peak activity during each 5

110   s window were frequently higher than those in the shuffled data (Figure 3–Figure supplement

111   2 and Table supplement 1). To determine whether the activity pattern across trials was stable

112   for individual neurons with peak activity during the pre-reward period, we calculated the

113   correlation coefficient between the times of peak activity of two randomly separated groups

114   of trials (Figure 3–Figure supplement 3a, b; see details in Materials and Methods section) and

115   found that it was higher in the deep area than in the superficial area (Figure 3–Figure

116   supplement 3c). This suggests that the PL neurons reliably code the reward prediction (or

117   prediction of timing of the water delivery). The deep imaging method should therefore help

118   us to understand the hierarchical and/or parallel processing occurring across the M2 and PL

119   areas during decision-making.

120   We also examined the activity pattern of hippocampal CA1 neurons in the young

121   mice during the conditioning session (Video 4). The distribution of the time of peak activity

122   was not random in all neurons, but was random in those neurons with a peak activity during

7

123   the pre-reward period (Figure 4a–d). The time of peak activity of the latter neurons was also

124   unstable across trials (Figure 4e). This indicates that the hippocampal CA1 neurons do not

125   code the reward prediction in this conditioning without environmental changes, although we

126   could not exclude the possibility that reward prediction-related activity may mature in

127   adulthood.

128   In the intact brain, it is easy to change the field of view horizontally to the cortical

129   surface. An 8 mm-wide glass window can be used for long-term imaging of the whole dorsal

130   neocortex in the mouse (Kim et al., 2016), which would make it possible to image the medial

131   prefrontal cortex and the hippocampus in memory-guided decision-making. If an objective

132   with a wide field of view (>3 mm) is used (Sofroniew et al., 2016; Stirman et al., 2016; Tsai

133   et al., 2015), the neural activity in both areas could be simultaneously imaged. Deep and

134   wide-field two-photon calcium imaging of the intact brain will substantially help us

135   understand the brain circuits that underlie cognition and memory processes.

136

137

138   **Competing interests**

139   The authors declare no competing financial interests.

140

Author contributions

142   M.K. and M.M. designed the experiments. M.K. performed two-photon imaging and mouse

143   experiments and analyzed the data. M.O. and J. N. created R-CaMP1.07. K.K. made

144   AAV1-hSyn-R-CaMP1.07. M.K. and M.M. wrote the paper, with comments from all the

145   authors.

9

156   (Brain/MINDS) from Japan Agency for Medical Research and Development to M.M., and a

157   Takeda Foundation grant to M.M.

158

159   **Materials and Methods**

160   **Animals**

161   All animal experiments were approved by the Institutional Animal Care and Use Committee

162   of The University of Tokyo, Japan. All mice were provided with food and water *ad libitum*

163   and housed in a 12:12 h light–dark cycle. The mice were not used for other experiments

164   before this study. Male C57BL/6 mice (aged 2–3 months, SLC, Shizuoka, Japan) were

165   utilized for mFrC imaging. Male and female C57BL/6 mice (aged 12–40 days in the young

166   mice, and 2–3 months in the adult mice; Japan SLC, Shizuoka, Japan) were utilized for the

167   imaging experiments on the hippocampus. For experiments using young mice, pups were

168   weaned at P30, and then group-housed until the imaging window was implanted.

169

170   **Virus production**

171   In this study, two red-fluorescent genetically encoded calcium indicators, R-CaMP1.07

172   (Ohkura et al., 2012) and jRGECO1a (Dana et al., 2016), were used. For imaging of

173   R-CaMP1.07, the GCaMP3 DNA of pAAV-human synapsin I promoter

174   (hSyn)-GCaMP3-WPRE-hGH polyA (Masamizu et al., 2014) was replaced with

175   R-CaMP1.07 DNA from a pN1-R-CaMP1.07 vector construct (Ohkura et al., 2012).

11

176   rAAV2/1-hSyn-R-CaMP1.07 (1.3×10^{13} vector genomes/ml) was produced with pAAV2-1

177   and purified as described previously (Kaneda et al., 2011; Kobayashi et al., 2016).

178   rAAV2/1-hSyn-NES-jRGECO1a (2.95×10^{13} vector genomes/ml) was obtained from the

179   University of Pennsylvania Gene Therapy Program Vector Core.

180

181   **Surgical procedures**

182   *mFrC*

183   Mice were anesthetized by intramuscular injection of ketamine (74 mg/kg) and xylazine

184   (10 mg/kg) before an incision was made in the skin covering the neocortex. After the mice

185   were anesthetized, atropine (0.5 mg/kg) was injected to reduce bronchial secretion and

186   improve breathing, and an eye ointment (Tarivid; 0.3% w/v ofloxacin, Santen Pharmaceutical,

187   Osaka, Japan) was applied to prevent eye-drying. Body temperature was maintained at 36–

188   37°C with a heating pad. After the exposed skull was cleaned, a head-plate (Tsukasa Giken,

189   Shizuoka, Japan; Hira et al., 2013) was attached to the skull using dental cement (Fuji lute

190   BC; GC, Tokyo, Japan, and Bistite II; Tokuyama Dental, Tokyo, Japan). The surface of the

191   intact skull was coated with dental adhesive resin cement (Super bond; Sun Medical, Shiga,

192   Japan) to prevent drying. An isotonic saline solution with 5 w/v% glucose was injected

12

193   intraperitoneally after the surgery. Mice were allowed to recover for 1 day before virus

194   injection.

195   Thirty minutes before surgery for virus injection, dexamethasone sodium

196   phosphate (1.32 mg/kg) was administered intraperitoneally to prevent cerebral edema. Mice

197   were anesthetized with isoflurane (3–4% for induction and ~1% during surgery) inhalation

198   and placed on a stereotaxic frame (SR-5M; Narishige, Tokyo, Japan). Before virus injection,

199   a pulled glass pipette (broken and beveled to an outer diameter of 25–30 μm; Sutter

200   Instruments, CA, USA) and a 5 μl Hamilton syringe were back-filled with mineral oil

201   (Nacalai Tesque, Kyoto, Japan) and front-loaded with virus solution. The virus solution was

202   then injected into the mFrC (2.7–2.8 mm anterior and 0.4 mm left of the bregma, 800–1200

203   μm dorsal from the pial surface). To minimize background fluorescence from solution

204   backflow through the space made by the glass capillary insertion, the axis of the glass

205   capillary was angled 30–40° from the horizontal plane. From 100 to 200 nl of AAV solution

206   was injected via a syringe pump at a rate of 15–20 nl/min (KDS310; KD Scientific, MA,

207   USA). The capillary was maintained in place for more than 10 min after the injection before

208   being slowly withdrawn. The craniotomy was then covered with silicon elastomer (quick cast,

209   World Precision Instruments, FL, USA) and dental adhesive (Super bond). At least 3 weeks

13

210   after the viral injection, the craniotomy (1.5 mm diameter at the area of interest) was

211   conducted and dura mater was removed. A glass window was placed over the craniotomy,

212   and the edge was sealed with cyanoacrylate adhesive (Vetbond, 3M, MN, USA), dental resin

213   cement, and dental adhesive. The glass window consisted of two circular cover slips (No.1,

214   0.12–0.17 mm thickness and 2.5 mm diameter; and No.5, 0.45–0.60 mm thickness and 1.5

215   mm diameter; Matsunami Glass, Osaka, Japan) that were glued together with UV-curing

216   optical adhesive (NOR-61; Norland Products, NJ, USA). After the window implantation, a

217   250 μl saline solution containing anti-inflammatory and analgesic carprofen (6 mg/kg) was

218   administered intraperitoneally. Mice were then returned to their cages, and imaging sessions

219   were started after allowing at least 1 day for recovery.

220   *Hippocampus*

221   The procedures for the hippocampus were mostly the same as those for the mFrC. However,

222   when the viral solution was injected at P12–14, the head-plate was not attached, as at their

223   age the body size was too small to allow attachment. Two weeks after injection, the mice

224   were anesthetized by intraperitoneal injection of ketamine (74 mg/kg) and xylazine

225   (10 mg/kg), the head-plate was attached, and the imaging window was implanted. The glass

226   window consisted of two circular cover slips (No.1, 0.12–0.17 mm thickness and 2.5 mm

14

227   diameter; and No.3, 0.25–0.35 mm thickness and 1.5 mm diameter). The dura mater was not

228   removed, as it was thinner and more fragile than that in the adult mice.

229

230   **Behavioral conditioning**

231   The mice were water-deprived in their home cages and maintained at 80–85% of their normal

232   weight throughout the experiments. During the behavioral conditioning, mice were set within

233   a body chamber and head-fixed with custom-designed apparatus (O'Hara, Tokyo, Japan; Hira

234   et al., 2013). A spout was set in front of their mouth, and a 4 µl drop of water was delivered

235   from the spout at a time interval of 20 s. The mice were allowed to lick at any time, and

236   licking behavior was monitored by an infrared LED sensor. The rate of water delivery that

237   incurred at least one lick during 2 s after the delivery was defined as the responsive rate. The

238   duration of the daily conditioning sessions was 40–60 min. At the end of each session, the

239   mice were allowed to freely gain water drops (total water consumption was ~1 ml per

240   session). On rest days (typically weekends), the mice had free access to a 3% agarose block

241   (1.2 g per day) in the cage.

242

243   **Two-photon calcium imaging**

15

244   Two-photon imaging was conducted using an FVMPE-RS system (Olympus, Tokyo, Japan)

245   equipped with a 25× water immersion objective (for imaging of the mFrC:

246   XLPLN25XSVMP, numerical aperture: 1.0, working distance: 4 mm, Olympus; for imaging

247   of the hippocampus: XLPLN23XWMP2, numerical aperture: 1.05, working distance: 2 mm,

248   Olympus) and a broadly tunable laser with a pulse width of 120 fs and a repetition rate of 80

249   MHz (Insight DS+ Dual, Spectra Physics, CA, USA), set at a wavelength of 1100 nm.

250   Fluorescence emissions were collected using a GaAsP photomultiplier tube (Hamamatsu

251   Photonics, Shizuoka, Japan). To shorten the light-path length within the tissue, the back

252   aperture of the objective was underfilled with the diameter-shortened (7.2 mm, in comparison

253   with that of the back aperture of 15.1 mm or 14.4 mm) laser beam[11]. When the modified laser

254   at a wavelength of 1100 nm was used for two-photon excitation of 0.1 μm fluorescent beads,

255   the full-widths at half-maximum were 0.94 ± 0.09 μm (mean ± s.d., $n = 5$ beads) laterally and

256   7.7 ± 1.70 μm ($n = 5$ beads) axially, which are comparable to those used for two-photon

257   calcium imaging of multiple neurons with cellular resolution (Lecoq et al., 2014; Sadakane et

258   al., 2015).

259   During the imaging session, the mouse head was fixed and the body was

260   constrained within a body chamber under the microscope (OPR-GST, O'Hara; Masamizu et

16

261   al., 2014). Before the first imaging session of each mouse started, the angle of the stage on

262   which the mouse chamber was placed was finely adjusted to set the glass window

263   perpendicular to the optical axis. This was accomplished by the imaging of microbeads on the

264   surface of the glass window (Kawakami et al., 2015). The frame acquisition rate was 30

265   frames/s, and the size of the imaging fields was generally 512×512 pixels (0.904 μm/pixel),

266   or 512×160 pixels, with three-frame averaging to increase the signal-to-noise ratio. The

267   depth of the functional imaging plane was up to 1200 μm from the cortical surface ($n = 62$

268   planes in the mFrC from 11 mice expressing R-CaMP1.07, $n = 6$ in the hippocampus from

269   three mice expressing jRGECO1a). The duration of one imaging session was 15–20 min, and

270   1–4 imaging sessions from different depths were performed in a daily experiment. For each

271   mouse, imaging was conducted for 3–5 days.

272

273   **Image processing**

274   Analyses were performed using MATLAB (R2016a, version 9.0.0.341360; MathWorks, MA,

275   USA) and Fiji software (Schindelin et al., 2012). Raw image sequences acquired on the

276   FVMPE-RS system were loaded into MATLAB using custom-written scripts. Motion

277   correction was performed by phase-correlation using the Suite2P package (Pachitariu et al.,

17

278   2016). After the motion correction, images were three frame-averaged before being analyzed.

279   A constrained non-negative matrix factorization (cNMF) algorithm was employed to extract

280   neural activities from a time series of images (Pnevmatikakis et al., 2016). The noise

281   variances in the power spectrum density at high frequency estimated by the cNMF algorithm

282   were as follows (mean ± s.d.): 14.42 ± 5.11 ($n = 12$ fields) in the superficial area of the mFrC,

283   22.00 ± 10.27 ($n = 35$ fields) in the middle area of the mFrC, 21.69 ± 12.63 ($n = 15$ fields) in

284   the deep area of the mFrC, and 19.45 ± 3.68 ($n = 6$ fields) in the hippocampal CA1 region.

285   The detrended relative fluorescence changes ($\Delta F/F$) were calculated with eight percentile

286   values over an interval of ± 30 s around each sample time point (Dombeck et al., 2007).

287   Traces of $\Delta F/F$ from 10 s before to 10 s after the water delivery in those deliveries with at

288   least one lick during 2 s after the delivery were used for the analyses.

289

290   **Data analysis**

291   The ridge-to-background ratio was used for the estimation of the distribution of the time of

292   peak activity (Harvey et al., 2012). To create a shuffled $\Delta F/F$ trace of each neuron, the time

293   point of the actual $\Delta F/F$ trace was circularly shifted by a random amount for each trial and

294   then trial-averaged. For each neuron, the ridge $\Delta F/F$ was defined as the mean $\Delta F/F$ over 12

18

295   frames (100 ms/frame) surrounding the time of peak activity, and the background $\Delta F/F$ was

296   defined as the mean $\Delta F/F$ in the other data points. The ridge $\Delta F/F$ was then divided by the

297   background $\Delta F/F$.

298   The trial-by-trial stability of the time of peak activity of the neurons that had their

299   peak activity during the pre-reward period (-10 s to 0 s) was evaluated as follows: in each

300   session, all trials were randomly divided into two groups, and the trial-averaged activity in

301   each group was calculated for each neuron. To remove the effects of different sample sizes

302   across the three mFrC areas and the hippocampus, 50 neurons were randomly chosen from all

303   imaging fields in each area. The time of peak activity in one group was plotted against that in

304   the other, and the Pearson's correlation coefficient was determined. Thus, if the timing of the

305   peak activity of each neuron was constant across trials, the correlation coefficient should be 1.

306   This procedure was repeated 1000 times, and the 95% confidence interval was determined for

307   each of the areas. When the lower bound of the 95% confidence interval was above zero, it

308   was concluded that the time of peak activity was not random across trials. To estimate the

309   difference in the trial-by-trial stability of the time of peak activity between pairs of the three

310   areas in the mFrC (Figure 3–Figure supplement 3c), the mean correlation coefficients were

311   compared using a permutation test. For each pair from the superficial, middle, and deep areas,

19

312   all neurons with peak activity during the pre-reward period were randomly reassigned to one

313   of the two areas. For each area with reassigned neurons, the correlation coefficient between

314   the times of peak activity of the two randomly separated groups of trials was calculated, and

315   the absolute difference of the correlation coefficients between the two areas was estimated.

316   This procedure was repeated 10000 times, and the distribution of the absolute differences

317   between the two areas was determined. Following this, the statistical significance was

318   determined according to whether or not the absolute difference in the mean correlation

319   coefficients between the two areas with original neurons assigned (Figure 3–Figure

320   supplement 3b) was above the 95th percentile of the resampled distribution corrected using

321   the Bonferroni method.

322

323   **Histology**

324   After the last *in vivo* imaging session, the mice were deeply anesthetized with ketamine (74

325   mg/kg) and xylazine (10 mg/kg) and transcardially perfused with 40 ml of phosphate

326   buffered saline (PBS) and 40 ml of 4% paraformaldehyde in PBS (Wako, Osaka, Japan). The

327   brains were removed and postfixed with the same fixative at 4°C for longer than 12 h. For

328   immunostaining, the brains were cut into coronal sections with a thickness of 50–100 μm.

20

329   Slices were washed in PBS-X (0.5% triton-X in PBS) containing 10% normal goat serum,

330   and then incubated with one of the primary antibodies (1:500 dilution of rabbit anti-GFAP

331   [glial fibrillary acidic protein], G9269, Sigma-Aldrich, MO, USA; 1:500 dilution of rabbit

332   anti-Iba1, 019-19741, Wako; 1:400 dilution of mouse anti-HSP70/72 [heat shock protein

333   70/72], ADI-SPA-810-F, Enzo Life Sciences, NY, USA) overnight at 4°C. Afterwards, slices

334   were washed in PBS-X and incubated with species-appropriate Alexa Fluoro-488 conjugated

335   secondary antibody (1:500 dilution of anti-rabbit IgG for GFAP and Iba1 antibodies; 1:500

336   dilution of anti-mouse IgG for HSP70/72 antibody). After staining the cell nuclei with

337   fluorescent Nissl stain (NeuroTrace 435/455, 1:200, N21479, Thermo Fisher Scientific, MA,

338   USA), the slices were mounted on glass slides with Fluoromount/Plus mounting medium

339   (Diagnostic BioSystems, CA, USA). Fluorescence images were acquired with an upright

340   fluorescence microscope (BX53, Olympus) and a CCD camera (Retiga 2000R, Q Imaging,

341   BC, Canada), and analyzed with Fiji software (Schindelin et al., 2012).

342

343   **Statistics**

344   Data are presented as mean ± s.d., and the Wilcoxon rank-sum tests, Spearman's correlation

345   tests, Pearson's correlation tests, and permutation tests described above were used for

21

346   statistical comparisons. Pairwise comparisons were two-tailed unless otherwise noted. Error

347   bars in graphs represent the s.e.m. No statistical tests were run to predetermine the sample

348   size, and blinding and randomization were not performed.

349

350

351   **References**

352   Attardo A, Fitzgerald JE, Schnitzer MJ. 2015. Impermanence of dendritic spines in live adult CA1

353   hippocampus. *Nature* **523**: 592–596.

354   Dana H, Mohar B, Sun Y, Narayan S, Gordus A, Hasseman JP, Tsegaye G, Holt GT, Hu A, Walpita D,

355   Patel R, Macklin JJ, Bargmann CI, Ahrens MB, Schreiter ER, Jayaraman V, Looger LL,

356   Svoboda K, Kim DS. 2016. Sensitive red protein calcium indicators for imaging neural

357   activity. *eLife* **5**: 413.

358   Dombeck DA, Harvey CD, Tian L, Looger LL, Tank DW. 2010. Functional imaging of hippocampal

359   place cells at cellular resolution during virtual navigation. *Nature Neuroscience* **13**: 1433–

360   1440.

361   Dombeck DA, Khabbaz AN, Collman F, Adelman TL, Tank DW. 2007. Imaging large-scale neural

362   activity with cellular resolution in awake, mobile mice. *Neuron* **56**: 43–57.

363   Friedman A, Homma D, Gibb LG, Amemori K, Rubin SJ, Hood AS, Riad MH, Graybiel AM. 2015. A

364   Corticostriatal path targeting striosomes controls decision-making under conflict. *Cell* **161**:

365   1320–1333.

366   Harvey CD, Coen P, Tank DW. 2012. Choice-specific sequences in parietal cortex during a

367   virtual-navigation decision task. *Nature* **484**: 62–68.

23

368   Helmchen F, Denk W. 2005. Deep tissue two-photon microscopy. *Nature Methods* **2**: 932–940.

369   Hira R, Ohkubo F, Ozawa K, Isomura Y, Kitamura K, Kano M, Kasai H, Matsuzaki M. 2013.

370   Spatiotemporal dynamics of functional clusters of neurons in the mouse motor cortex during a

371   voluntary movement. *Journal of Neuroscience* **33**: 1377–1390.

372   Inoue M, Takeuchi A, Horigane S, Ohkura M, Gengyo-Ando K, Fujii H, Kamijo S, Takemoto-Kimura

373   S, Kano M, Nakai J, Kitamura K, Bito H. 2014. Rational design of a high-affinity, fast, red

374   calcium indicator R-CaMP2. *Nature Methods* **12**: 64–70.

375   Ji N, Milkie DE, Betzig, E. 2010. Adaptive optics via pupil segmentation for high-resolution imaging

376   in biological tissues. *Nature Methods* **7**: 141–147.

377   Jia H, Rochefort NL, Chen X, Konnerth A. 2010. Dendritic organization of sensory input to cortical

378   neurons *in vivo*. *Nature* **464**: 1307–1312.

379   Kaneda K, Kasahara H, Matsui R, Katoh T, Mizukami H, Ozawa K, Watanabe D, Isa T. 2011.

380   Selective optical control of synaptic transmission in the subcortical visual pathway by

381   activation of viral vector-expressed halorhodopsin. *PLoS One* **6**: e18452.

382   Kawakami R, Sawada K, Sato A, Hibi T, Kozawa Y, Sato S, Yokoyama H, Nemoto T. 2013.

383   Visualizing hippocampal neurons with *in vivo* two-photon microscopy using a 1030 nm

384   picosecond pulse laser. *Scientific Reports* **3**: 1–7.

24

385   Kawakami R, Sawada K, Kusama Y, Fang YC, Kanazawa S, Kozawa Y, Sato S, Yokoyama H,

386   Nemoto T. 2015. *In vivo* two-photon imaging of mouse hippocampal neurons in dentate gyrus

387   using a light source based on a high-peak power gain-switched laser diode. *Biomedical Optics*

388   *Express* **6**: 891–901.

389   Kim H, Ährlund-Richter S, Wang X, Deisseroth K, Carlén M. 2016. Prefrontal parvalbumin neurons

390   in control of attention. *Cell* **164**: 208–218.

391   Kim TH, Zhang Y, Lecoq J, Jung JC, Li J, Zeng H, Niell CM, Schnitzer MJ. 2016. Long-term optical

392   access to an estimated one million neurons in the live mouse cortex. *Cell Reports* **17**: 3385–

393   3394.

394   Kobayashi K, Sano H, Kato S, Kuroda K, Nakamuta S, Isa T, Nambu A, Kaibuchi K, Kobayashi K.

395   2016. Survival of corticostriatal neurons by Rho/Rho-kinase signaling pathway. *Neuroscience*

396   *Letters* **630**: 45–52.

397   Lecoq J, Savall J, Vučinić D, Grewe BF, Kim H, Li JZ, Kitch LJ, Schnitzer MJ. 2014. Visualizing

398   mammalian brain area interactions by dual-axis two-photon calcium imaging. *Nature*

399   *Neuroscience* **17**: 1825–1829.

400   Low RJ, Gu Y, Tank DW. 2014. Cellular resolution optical access to brain regions in fissures:

401   imaging medial prefrontal cortex and grid cells in entorhinal cortex. *Proceedings of the*

402   *National Academy of Sciences of the United States of America* **111**: 18739–18744.

403   Masamizu Y, Tanaka YR, Tanaka YH, Hira R, Ohkubo F, Kitamura K, Isomura Y, Okada T,

404   Matsuzaki M. 2014. Two distinct layer-specific dynamics of cortical ensembles during

405   learning of a motor task. *Nature Neuroscience* **17**: 987–994.

406   Matsuzaki M, Ellis-Davies GCR, Kasai H. 2008. Three-dimensional mapping of unitary synaptic

407   connections by two-photon macro photolysis of caged glutamate. *Journal of Neurophysiology*

408   **99**: 1535–1544.

409   Ohkura M, Sasaki T, Kobayashi C, Ikegaya Y, Nakai J. 2012. An improved genetically encoded red

410   fluorescent Ca^{2+} indicator for detecting optically evoked action potentials. *PLoS One* **7**:

411   e39933.

412   Ohki K, Chung S, Ch'ng YH, Kara P, Reid RC. 2005. Functional imaging with cellular resolution

413   reveals precise micro-architecture in visual cortex. *Nature* **433**: 597–603.

414   Pachitariu M, Stringer C, Schröder S, Dipoppa M, Rossi LF, Carandini M, Harris KD. 2016. Suite2p:

415   beyond 10,000 neurons with standard two-photon microscopy. *bioRxiv*, doi:10.1101/061507.

26

416   Paxinos G and Franklin K. 2007. *The mouse brain in stereotaxic coordinates* (3rd edition, Academic

417   Press).

418   Pilz GA, Carta S, Stäuble A, Ayaz A, Jessberger S, Helmchen F. 2016. Functional imaging of dentate

419   granule cells in the adult mouse hippocampus. *Journal of Neuroscience* **36**: 7407–7414.

420   Pinto L, Dan Y. 2015. Cell-Type-Specific Activity in Prefrontal Cortex during Goal-Directed

421   Behavior. *Neuron* **87**: 437–450.

422   Pnevmatikakis EA, Soudry D, Gao Y, Machado TA, Merel J, Pfau D, Reardon T, Mu Y, Lacefield C,

423   Yang W, Ahrens M, Bruno R, Jessell TM, Peterka DS, Yuste R, Paninski L. 2016.

424   Simultaneous denoising, deconvolution, and demixing of calcium imaging data. *Neuron* **89**:

425   285–299.

426   Podgorski K, Ranganathan G. 2016. Brain heating induced by near-infrared lasers during multiphoton

427   microscopy. *Journal of Neurophysiology* **116**: 1012–1023.

428   Sadakane O, Masamizu Y, Watakabe A, Terada S, Ohtsuka M, Takaji M, Mizukami H, Ozawa K,

429   Kawasaki H, Matsuzaki M, Yamamori T. 2015. Long-term two-photon calcium imaging of

430   neuronal populations with subcellular resolution in adult non-human primates. *Cell Reports*

431   **13**: 1989–1999.

432   Schindelin J, Arganda-Carreras I, Frise E, Kaynig V, Longair M, Pietzsch T, Preibisch S, Rueden C,

433   Saalfeld S, Schmid B, Tinevez JY, White DJ, Hartenstein V, Eliceiri K, Tomancak P, Cardona

434   A. 2012. Fiji: an open-source platform for biological-image analysis. *Nature Methods* **9**: 676–

435   682.

436   Sofroniew NJ, Flickinger D, King J, Svoboda K. 2016. A large field of view two-photon mesoscope

437   with subcellular resolution for *in vivo* imaging. *eLife* **5**: 413.

438   Stirman JN, Smith IT, Kudenov MW, Smith SL. 2016. Wide field-of-view, multi-region, two-photon

439   imaging of neuronal activity in the mammalian brain. *Nature Biotechnology*. **34**: 865–870.

440   Sul JH, Jo S, Lee D, Jung MW. 2011. Role of rodent secondary motor cortex in value-based action

441   selection. *Nature Neuroscience* **14**: 1202–1208.

442   Tischbirek C, Birkner A, Jia H, Sakmann B, Konnerth A. 2015. Deep two-photon brain imaging with

443   a red-shifted fluorometric Ca^{2+} indicator. *Proceedings of the National Academy of Sciences of*

444   *the United States of America* **112**: 11377–11382.

445   Tsai PS, Mateo C, Field JJ, Schaffer CB, Anderson ME, Kleinfeld D. 2015. Ultra-large field-of-view

446   two-photon microscopy. *Optics Express* **23**: 13833–15.

447

448   **Figure Legends**

449   **Figure 1. | Optical access to intact medial frontal cortex.**

450   (**a**) Schematic illustration of *in vivo* two-photon imaging of the mFrC. The dotted square

451   indicates the location where the Z-stack images, as in (**b**), were acquired. FrC, frontal cortex;

452   PL, prelimbic area. (**b**) Representative XZ image of mFrC expressing R-CaMP1.07. Scale bar,

453   200 μm. (**c**) Left, top: representative time-averaged XY image of mFrC expressing

454   R-CaMP1.07 at a depth of 1030 μm. Scale bar, 100 μm. Left, bottom: spatial distribution of

455   identified neurons. Traces of the calcium transients of the numbered filled circles are shown

456   on the right. (**d**) Expression of R-CaMP1.07 (red) and cell nuclei (NeuroTrace 435, cyan)

457   after imaging of 11 fields at depths of 340–1140 μm for 5 days. The total duration of imaging

458   was 200 min. There is no apparent abnormality of fluorescence expression in the mFrC. Scale

459   bar, 1 mm. (**e**–**g**) Expressions of GFAP (**e**), Iba1 (**f**), and HSP70/72 (**g**) in contra-lateral (left)

460   and imaged (right) hemispheres from the same mouse imaged in (**d**). Only slight glial

461   activation and heat shock reactivity was observed. Scale bar, 1 mm.

462

463   **Figure 2. | Optical access to hippocampal CA1 region in the intact brain.**

464   (**a**) Schematic illustration of *in vivo* two-photon imaging of the hippocampal CA1 region. The

465   dotted square indicates the location where Z-stack images, as in (**b**), were acquired. (**b**)

29

466   Representative XZ image of jRGECO1a-expressing hippocampus and deep cortical layer.

467   Scale bar, 200 μm. (**c**) Left, top: representative time-averaged XY image of

468   jRGECO1a-expressing CA1 pyramidal layer at a depth of 1040 μm from the cortical surface.

469   Scale bar, 100 μm. Dense distribution of CA1 neurons is apparent when the images are

470   time-averaged. Left, bottom: spatial distribution of identified neurons. Traces of the calcium

471   transients of the numbered filled circles are shown on the right. (**d**) Expression of jRGECO1a

472   and cell nuclei after 40 min (in total) imaging of the hippocampal CA1 region for 2 days.

473   Scale bar, 1 mm. (**e**) Expressions of GFAP (left), Iba1 (middle), or HSP70/72 (right) in the

474   contra-lateral and imaged hemispheres from the same mouse imaged in (**d**). Scale bar, 1 mm.

475

476   **Figure 3. | Neural activity in the medial frontal cortex during conditioning.**

477   (**a**) Representative traces of licking behavior at conditioning sessions 1 (top) and 4 (bottom)

478   from the same mouse. Dashed-vertical lines indicate timings of water delivery. (**b**) Mean

479   traces of lick frequency at sessions 1 (red) and 4 (blue; $n = 11$ mice). Light shading indicates

480   the s.e.m. (**c**) Time course of responsive rate (rate of those deliveries with licking occurring

481   within 2 s after the delivery; $n = 11$ at sessions 1–4 and $n = 5$ at session 5 before imaging

482   started). (**d**) Time course of reaction time (time from the water delivery to the first lick). (**e**)

483   Normalized trial-averaged activity of each neuron aligned with the water delivery (dashed

30

484   lines) and ordered by the time of peak activity. Top, middle, and bottom panels are the

485   superficial (12 fields from 7 mice), middle (35 fields from 10 mice), and deep (15 fields from

486   7 mice) areas respectively. (**f**) Polar histograms of the time of peak activity from reward

487   delivery (red line). The time bin is 0.5 s, and they are ordered clockwise from the top (−10 s

488   to 10 s). (**g**) Normalized trial-averaged shuffled activity of each neuron. The shuffled activity

489   was calculated by circular shifts of the original calcium traces in each trial. (**h**) Distribution

490   and mean of the ridge-to-background ratios in original and shuffled datasets. Top to bottom

491   rows correspond to the superficial ($P = 4.81 \times 10^{-101}$, $n = 966$ neurons, Wilcoxon rank-sum

492   test), middle ($P = 4.34 \times 10^{-248}$, $n = 2612$ neurons), and deep areas ($P = 2.04 \times 10^{-146}$, $n = 983$

493   neurons). ***: $P < 0.001$.

494

495   **Figure 4. | Neural activity in the hippocampal CA1 region during conditioning.**

496   (**a**) Normalized trial-averaged activity of each neuron aligned with the water delivery (dashed

497   lines) and ordered by the time of peak activity. (**b**) Left, Normalized trial-averaged shuffled

498   activity of each neuron aligned with the water delivery timing and ordered by the time of

499   peak activity. Right, Distribution and mean of the ridge-to-background ratio in the original

500   and shuffled datasets. ***: $P = 0.000033$, $n = 133$ neurons, Wilcoxon rank-sum test. (**c**) Polar

501   histogram of the time of peak activity from reward delivery in each cell in the pooled data.

31

502   (**d**) Distribution and mean of the ridge-to-background ratio of neurons with peak activity

503   during the pre-reward period in original and shuffled datasets. $P = 0.28$, $n = 31$ neurons,

504   Wilcoxon rank-sum test. (**e**) Histograms of the correlation coefficients of the time of peak

505   activity between the two randomly divided groups of trials in neurons with peak activity

506   during the pre-reward period.

507

508

509   **Video 1. | Representative two-photon XYZ images of the mFrC expressing**
510   **R-CaMP1.07.**

511   The depth increment in the image stack was 2.0 μm, and the bottom depth of the imaging was

512   1100 μm. The field of view was 512×512 pixels with a size of 509.18 μm $\times$ 509.18 μm.

513   Each image was the average of 16 frames. The mouse was not anesthetized. The motion

514   correction was not conducted. The movie was denoised with a spatial Gaussian filter (σ =

515   0.6). The right image corresponds to XZ plane of the XYZ images (max intensity-projection

516   toward Y dimension) and the horizontal yellow line indicates the current depth of the left XY

517   image.

518

519   **Video 2. | Representative two-photon XYZ images of the neocortex and hippocampus**

520   **that expressed jRGECO1a.**

32

521   The depth increment in the image stack was 2.5 μm, and the bottom depth of the imaging was

522   1100 μm. The field of view was the same size as in Video 1. Each image was the average of

523   16 frames. The mouse was not anesthetized. The motion correction was not conducted. The

524   movie was denoised with a spatial Gaussian filter ($\sigma = 0.6$). The right image corresponds to

525   XZ plane of the XYZ images (max intensity-projection toward Y dimension) and the

526   horizontal yellow line indicates the current depth of the left XY image. Some leakage of the

527   virus from the hippocampus to the neocortex during the injection procedure may cause a

528   subset of the neocortical neurons to express jRGECO1a.

529

530   **Video 3. | Functional imaging of the PL area expressing R-CaMP1.07 during**

531   **conditioning.**

532   The imaging depth was 1100 μm from the cortical surface. The field of view was 509.18 μm

533     $\times$ 509.18 μm and 512 $\times$ 512 pixels. White circles at the right bottom indicate the timing of

534   water delivery, with an inter-delivery interval of 20 s. The data were acquired at 30 Hz, and

535   the movie was downsampled to 5 Hz and denoised with a spatio-temporal Gaussian filter

536   (spatial $\sigma = 0.6$, temporal $\sigma = 0.8$).

537

33

538 **Video 4. | Functional imaging of the hippocampal CA1 pyramidal layer that expressed**

539 **jRGECO1a during conditioning.**

540 The imaging depth was 1000 μm from the cortical surface, and the upper cortical tissue was

541 intact. The field of view was 509.18 μm × 159.04 μm and 512 × 160 pixels. White circles at

542 the right bottom indicate the timing of water delivery, with an inter-delivery interval of 20 s.

543 The data were acquired at 30 Hz (three frame-averaged), and the movie was downsampled to

544 5 Hz and denoised with a spatio-temporal Gaussian filter (spatial σ = 0.6, temporal σ = 0.8).

545
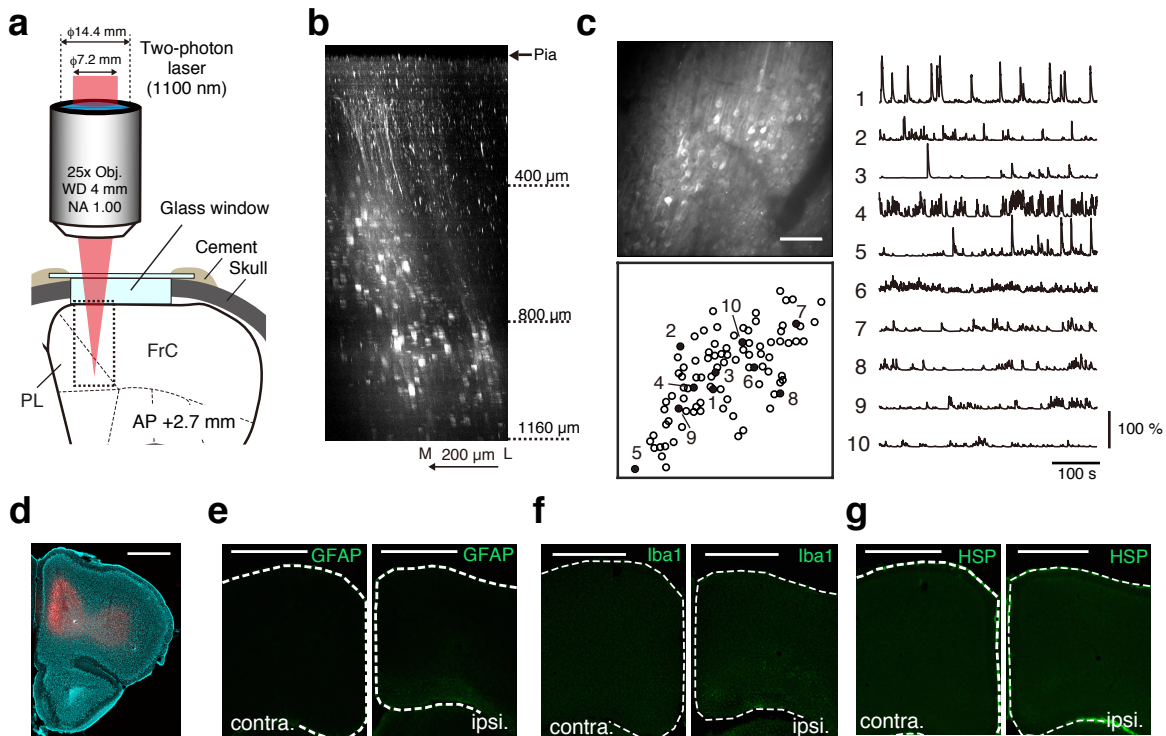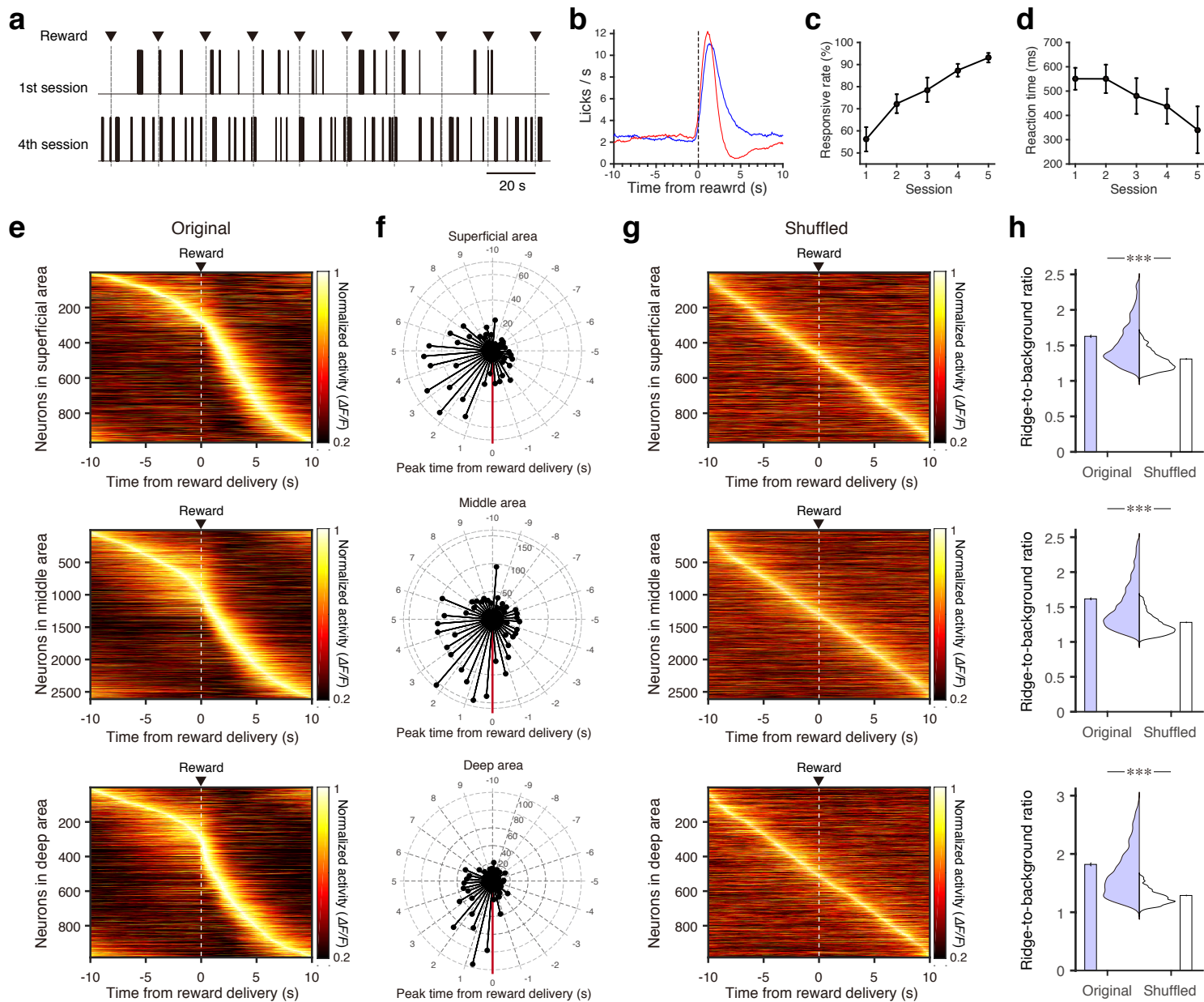
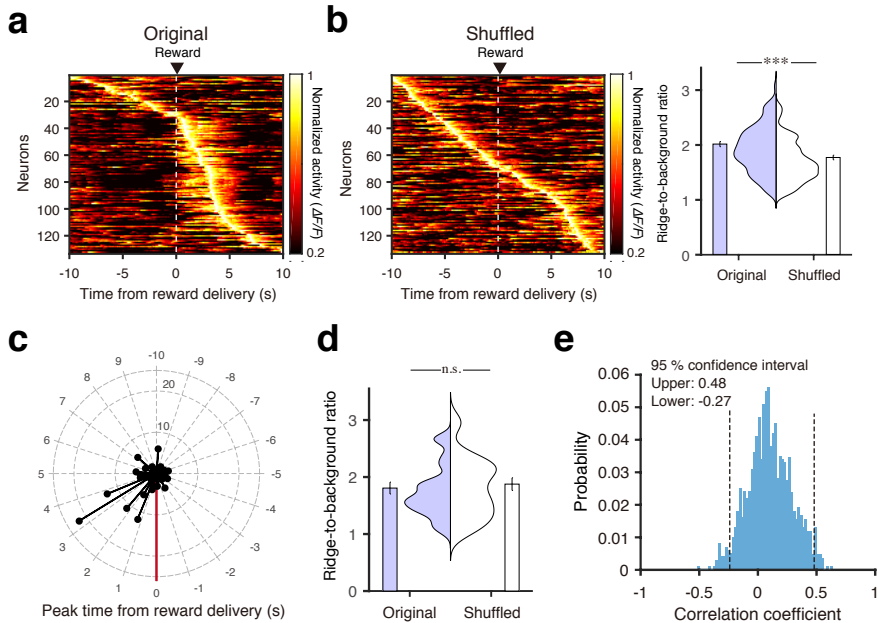Figure 1. Kondo et al.
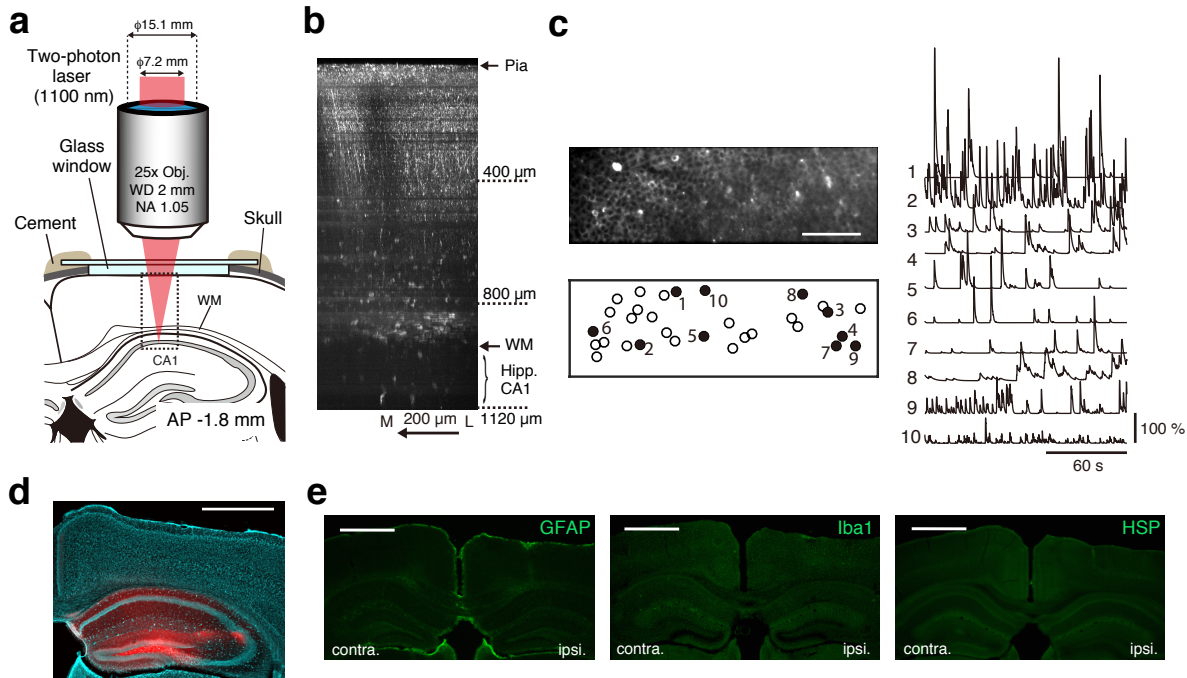
Figure 2. Kondo et al.

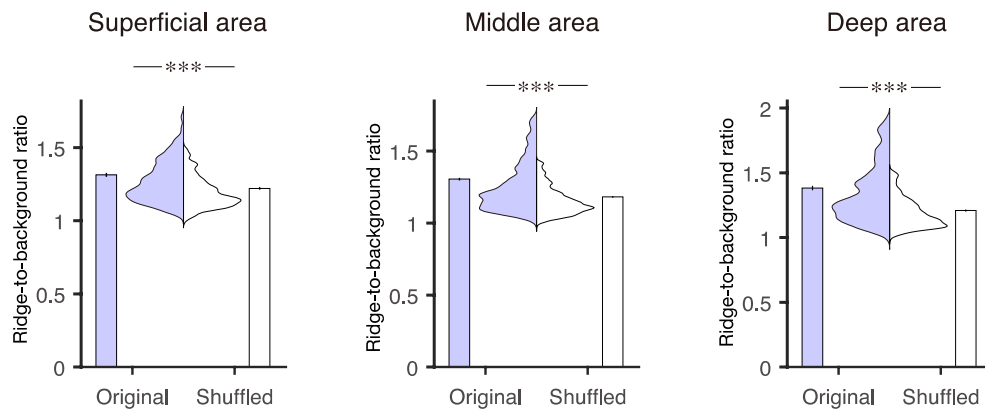Figure 3. Kondo et al.

Figure 4. Kondo et al.

Figure 3–Figure supplement 1. Kondo et al.

Figure 3–Figure supplement 1. | Ridge-to-background ratios of the mFrC neurons

showing peak activity during the pre-reward period.

Distribution and mean of the ridge-to-background ratios in original and shuffled datasets from neurons with peak activity during the pre-reward period. Left to right panels correspond to the superficial ($P = 1.99 \times 10^{-8}$, $n = 273$ neurons, Wilcoxon rank-sum test), middle ($P = 4.21 \times 10^{-37}$, $n = 943$ neurons), and deep areas ($P = 2.37 \times 10^{-17}$, $n = 286$ neurons). ***: $P < 0.001$.
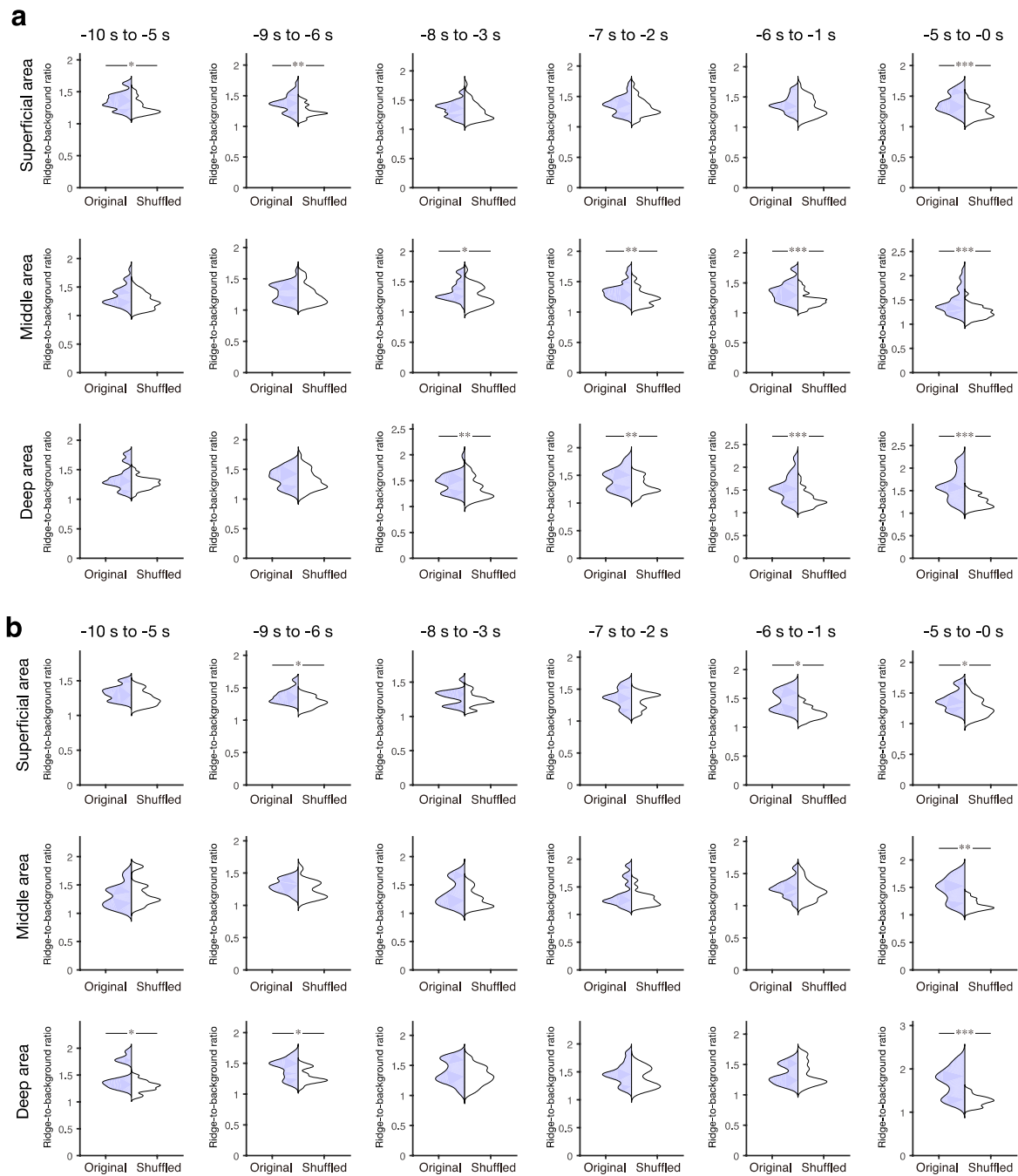
1

Figure 3–Figure supplement 2. Kondo et al.

Figure 3–Figure supplement 2. | Ridge-to-background ratios of neurons showing peak activity during 5 s windows in the pre-reward period.

(**a, b**) Examples of ridge-to-background ratios calculated from neurons with peak mean

activity occurring within six 5 s time windows (from left to right: −10 s to −5 s, −9 s to −4 s,

−8 s to −3 s, −7 s to −2 s, −6 s to −1 s, and −5 s to 0 s). Thirty-five (**a**) and fifteen (**b**) neurons

were randomly chosen to calculate the ratios. Top, middle, and bottom panels are the

superficial, middle, and deep areas of the mFrC, respectively. *: $P < 0.05$, **: $P < 0.01$, ***:
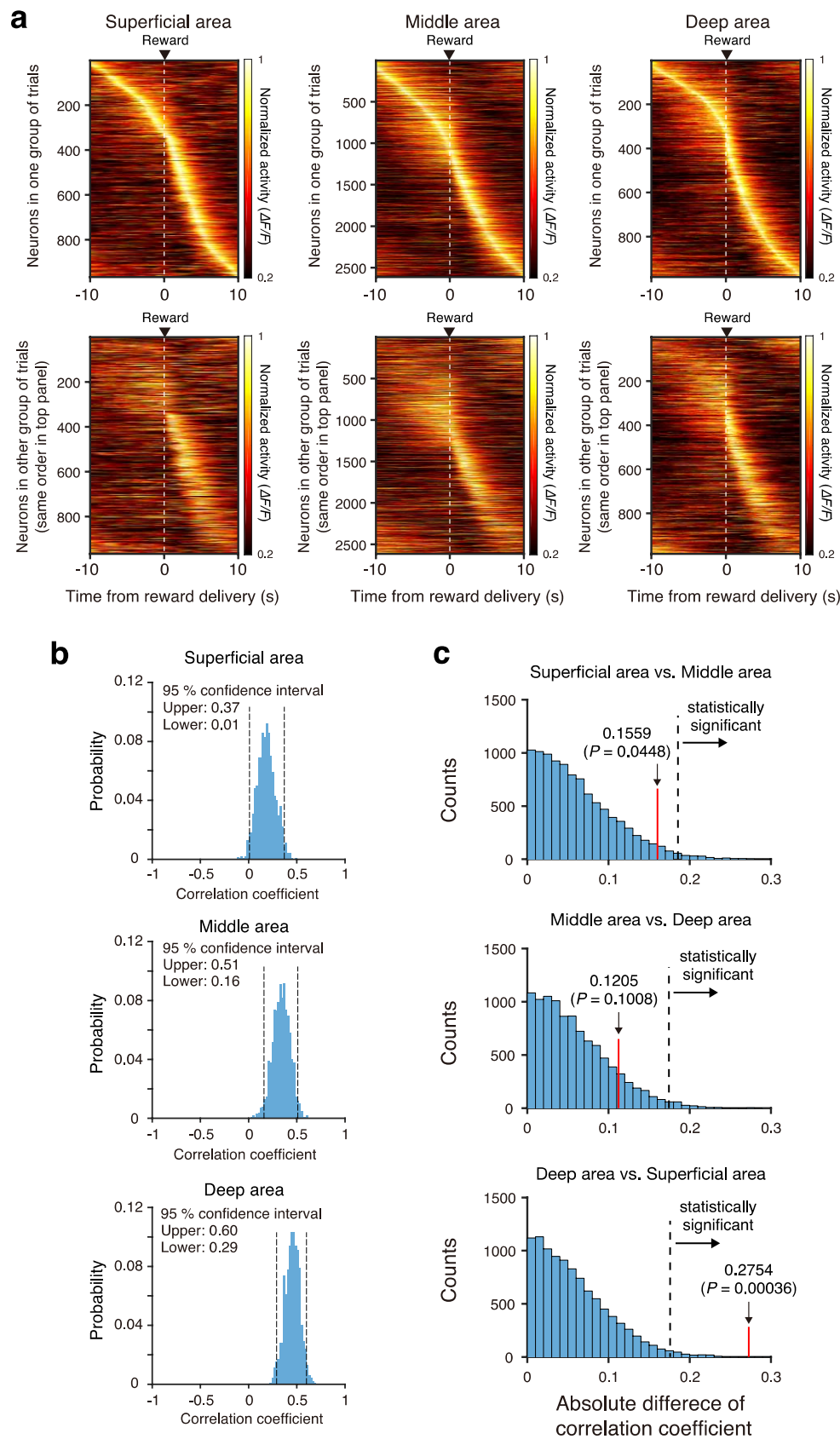
$P < 0.001$, Wilcoxon rank-sum test.

Figure 3–Figure supplement 3. Kondo et al.

Figure 3–Figure supplement 3. | Stability of trial-by-trial activity of the mFrC neurons with peak activity during the pre-reward period.

(**a**) Mean activity of mFrC neurons around the water delivery (dashed lines) from two representative separated groups of trials (top and bottom). In each column, neurons were ordered by the time of peak activity in the top group. A high similarity in the distribution between the top and bottom panels implies that trial-by-trial activity is stable. Left, the superficial area. Middle, the middle area. Right, the deep area. (**b**) Histograms of correlation coefficients of the time of peak activity between two randomly divided groups of trials, for those neurons with peak activity during the pre-reward period (-10 s to 0 s). The random division of trials was performed 1000 times (see details in Materials and Methods section).

(**c**) Distribution of the absolute difference of the correlation coefficient between two areas (top, superficial area vs. middle area; middle, middle area vs. deep area; bottom, deep area vs. superficial area) with randomly reassigned neurons with peak activity during the pre-reward period. The difference was estimated by a permutation procedure (see details in Data Analysis section in Materials and Methods). Dashed lines indicate 95th percentile corrected by the Bonferroni method (resulting in a 98.3% position). Red lines indicated the absolute differences of mean correlation coefficients calculated from (**b**). In the bottom subimage, the

5

red line is right of the dashed line, indicating that the trial-to-trial stability was statistically

higher in the deep area than in the superficial area.

(**a**) Randomly chosen 35 cells

(%)

Window Area	−10 s to −5 s	−9 s to −4 s	−8 s to −3 s	−7 s to −2 s	−6 s to −1 s	−5 s to 0 s
Superficial	30.91	27.30	15.30	17.37	51.06	77.31
Middle	38.69	43.64	45.65	57.45	75.61	88.24
Deep	59.74	47.66	27.64	49.66	82.95	96.99

(**b**) Randomly chosen 15 cells

(%)

Window Area	−10 s to −5 s	−9 s to −4 s	−8 s to −3 s	−7 s to −2 s	−6 s to −1 s	−5 s to 0 s
Superficial	9.20	7.51	5.14	5.01	14.81	25.96
Middle	11.61	12.79	13.01	17.10	26.66	37.30
Deep	17.26	12.94	7.44	12.96	28.54	50.20

Figure 3–Table supplement 1. | Statistics of ridge-to-background ratios of neurons showing peak activity during the 5 s windows in the pre-reward period.

Percentages of ridge-to-background ratios in which original data were significantly different ($P < 0.05$, Wilcoxon rank-sum test) from shuffled data. Random chooses of thirty-five (**a**) and fifteen (**b**) neurons to calculate the ratios were repeated 10000 times.